

FRACTURE PARAMETERS EVALUATION FOR THE CRACKED NONHOMOGENEOUS ENAMEL BASED ON THE FINITE ELEMENT METHOD AND VIRTUAL CRACK CLOSURE TECHNIQUE

Yan Cai^{1,2}, Liming Zhou¹, Ming Li¹

¹School of Mechanical and Aerospace Engineering, Jilin University, China

²Hospital of Stomatology, Jilin University, China

Abstract. *To accurately solve the fracture parameters of enamel, we have established computational nonhomogeneous enamel models and constructed the fracture element of enamel dumb nodes, based on the enamel mineral concentration, nonhomogeneous mechanical properties, and virtual crack closure technique. Through the commercial finite element software ABAQUS and the fracture element of the enamel dumb nodes, we have established the user subroutines UMAT and UEL, which enabled solving of the energy release rates of the nonhomogeneous enamel structure with cracks. The stress intensity factors of central cracks, three-point bend and compact stretched enamels, and double-edge notched stretched enamels are determined. By comparing them with analytical solutions, we have proved that the fracture element of the enamel dumb nodes is highly accurate, simple, and convenient. In addition, the cracks can be other elements rather than singular or special elements; they show versatility and other advantages. The stress intensity factor of the dental enamel can be solved more realistically. Thus, a new numerical method for prevention and treatment of dental diseases is provided.*

Key Words: *Nonhomogeneous Enamel Models, Crack, Virtual Crack Closure Technique, Finite Element Method, Fracture Element of Enamel Dumb Nodes*

1. INTRODUCTION

Enamel is the most important component of the outermost tissue of human teeth [1-3], which serves as a barrier for protecting the vital pulp and the dentin. On a microstructural level, a sequence of crystal rods (or “prisms”) with diameters of 4–6 μm compose the enamel tissue. The crystal rods stretch from the dentin-enamel-junction (DEJ) to the

Received June 19, 2021 / Accepted November 28, 2021

Corresponding author: Liming Zhou, Ming Li

School of Mechanical and Aerospace Engineering, Jilin University, Changchun, Jilin 130025, China

E-mail: lmzhou@jlu.edu.cn (Liming Zhou), liming940411@gmail.com (Ming Li).

occlusal surface and are arranged in a parallel manner [4]. The interface between the rods is a protein-rich district considered as the rod sheath. Enamel is a composite material that has a unique and complex hierarchical structure. The unique properties of enamel distinguish it from other biological tissues like bone or dentin [5]. In the body, enamel is the most highly mineralized tissue, being composed of approximately 96% minerals (primarily apatite crystals containing Ca^{2+} and P^{3-} , small amounts of other phosphate crystals, and small amounts of other minerals), and only 4% organic matrix and water (3% water and 1% proteins) by weight [6]. Teeth are well-designed to endure repeated chewing loads during a lifetime. To support oral function, the enamel should be equipped with adequate hardness, stiffness, and fracture resistance. Although the toughness of the protective enamel coat is comparable to that of glass, this material is highly brittle [7].

In dental clinic, incomplete tooth or tooth fracture is a general pathological feature [8, 9]. Considering the physiological characteristic of enamel and the circle force contact incurred during mastication, fatigue can lead to failure. Fractures that run as ribbon cracks around the enamel shell walls may occur as a result of macro-contacts in the cusp regions with hard millimeter-scale food objects (e.g., nuts, seeds, and hard particulates) [10-12]. These cracks are distributed along a normal direction to the tooth surface orientation and remain entirely contained within the enamel. Some cracks develop rapidly in clinic, and in severe cases, they can cause deterioration or even ultimate loss of tooth function. However, some fractured teeth can be used during life. Therefore, considering how to effectively protect the tooth activity and reduce or even block the propagation of cracks, further analysis of the mechanical characteristics of the dental enamel is required.

Over the last decade, enamel has been modeled as a homogenous material [13, 14], but recently, it has been explored with variations in its mechanical characteristics. Enamel hardness and elastic modulus decrease from the occlusal surface of enamel to the DEJ [15, 16]. The variations are probably due to chemistry, microstructure, and prism alignment. However, Cuy et al. [17] suggested that enamel is significantly correlated with changes in average chemistry: the concentrations of hydroxyapatites P_2O_5 and CaO are larger over the chewing surface and gradually decrease to the softer DEJ, but the concentrations of Na_2O and MgO change in the opposite direction. Braly [18] and Park [19] also reported similar variations of mechanical properties on the axial section of the enamel [20]. More recently, nanoindentation tests showed that the enamel elastic modulus and hardness decreased from ≥ 6 GPa and ≥ 120 GPa in the occlusal surface to less than 3 GPa and 70 GPa in the DEJ, respectively [21-23]. As reported, the crack growth resistance of enamel increases (rising R-curve) with crack extension from the outer to inner part; the law of variation of toughness is associated with the distance to DEJ [24].

Due to the small size of cracks, it is difficult to build an in-vitro experimental model for early cracked teeth. Thus, the finite element method (FEM) becomes relatively practical for studies on cracked teeth [25-27]. Recently, FEM has been widely used to analyze the causes of cracked teeth, but the existing studies have focused on the stress distribution, biomechanical factors, crack expanding behavior, and fatigue life of cracked teeth [28-30]. Moreover, due to methodological limitations, previous studies mostly regarded enamel as an isotropic material for mechanical analyses.

Using the analytical method, the fracture parameters of a simple geometric structure or a special load form of homogenous materials can be derived [31-33]. However, this method cannot be applied to complex systems or boundary conditions, as the calculation process

becomes very expensive and time-consuming. Nevertheless, these limitations can be overcome by using other numerical methods.

Nowadays, FEM is extensively employed in fracture analysis of nonhomogeneous materials. The elastic modulus coefficient of nonhomogeneous materials is a smoothing function of specific coordinates, also associated with the establishment of element stiffness matrix. For two-dimensional (2D) problems, the stress intensity factors for modes (modes I and II) can be comparatively evaluated through three nonhomogeneous material-tailored approaches: path-independent J-integral, virtual crack closure technique (VCCT) [34-37], and displacement correlation.

VCCT was used for 2D cracked specimens and thereafter expanded to three-dimensional crack problems [38-40]. Then, a method combining FEM and VCCT for the study of kinking cracks in a homogeneous material was introduced [41-43]. The energy release rates for cracks were computed by VCCT [44], and the interface cracks were studied with the virtual crack extension method and VCCT [45-47]. Krueger [48] presented an overview of the VCCT historical developments and discussed its different applications. Leski [49] provided the general conditions for implementation of VCCT in MSC.PATRAN.

Azimi et al. [50] probed into the special cracked lap shear specimen deboning using VCCT. Zeng et al. [51] extended VCCT to investigate the fracture mechanics parameters and simulate crack propagation within the framework of cell-based smoothed FEM. Banks-Sills and Farkash [52] explored VCCT to calculate stress intensity factors of two modes (modes I and II) for an interface crack between two linear elastic, isotropic, and homogeneous materials. VCCT was also extended to the investigation of the element-free Galerkin method [53, 54]. Based on graded FEM, a 2D-VCCT interface element was proposed for the dynamic fracture analysis issues [55].

Despite the secondary development of the commercial finite element software (ANSYS or ABAQUS), the crack problem analysis is mainly focused on homogeneous materials, and rarely on nonhomogeneous materials [56-58].

In this study, we built nonhomogeneous enamel models based on the commercial finite element analysis (FEA) software ABAQUS and VCCT. A dummy node enamel fracture element was established, and the energy release rates of nonhomogeneous cracked enamel were solved. The method provided better results compared to the analytical method in addressing nonhomogeneous mechanical properties.

2. MATERIALS AND METHODS

2.1. Nonhomogeneous enamel model

Previous studies mostly considered the enamel as an isotropic material for mechanical analysis. However, the tooth mineral concentrations gradually change from tooth surfaces to the DEJ [17] (Fig. 1). Based on Ref. [17], enamel is a nonhomogeneous material (from tooth surfaces to DEJ, the percentages of P_2O_5 , CaO, Na_2O , MgO and other components change in certain functions). For the model proposed, two materials were considered: Material C, with a composition of 94% $P_2O_5 + CaO$, 6% $Na_2O + MgO$ and other components, and material M, with a composition of 89% $P_2O_5 + CaO$, 11% $Na_2O + MgO$

and other components. Fig. 2 shows the gradient model of nonhomogeneous enamel materials. The enamels analyzed were composed of materials M and C, whose volume fractions continuously changed along certain dimensions of the model (Fig. 2). The Mori-Tanaka models and the rule of mixture are common methods to evaluate the effective elastic properties of grade composites. The effective moduli of the two materials were homogenized through these two methods. The effective property associated with volume fraction exponent follows a power law:

$$P(z) = P_m V_m + P_c V_c, V_m = 1 - V_c \quad (1)$$

$$V_c = (0.5 + z/h)^n, (-h/2 \leq z \leq h/2, 0 \leq n \leq \infty) \quad (2)$$

where subscripts m and c in Eq. (1) denote materials M and C, respectively; P denotes the Poisson's ratio or Young's modulus; z denotes the thickness coordinate; n is the power exponent factor. Eq. (1) presents the volume fraction variation along non-dimensional thickness (z/h). Volume fraction V_c variation with different power exponent factors n is shown in Fig. 3.

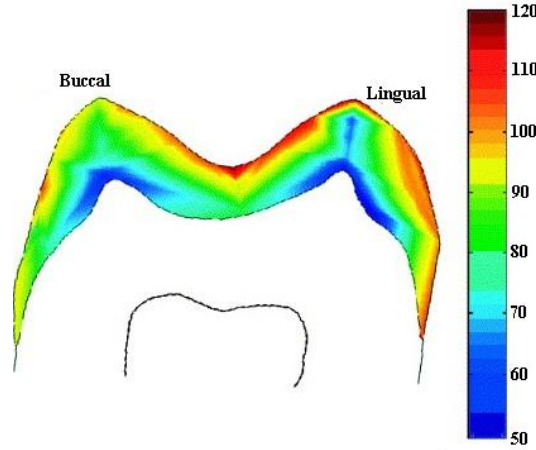


Fig. 1 Map of Young's modulus throughout the enamel by nanoindentation

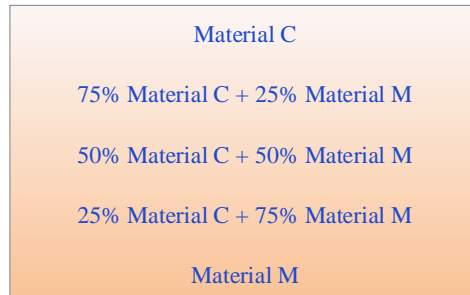


Fig. 2 Gradient model of nonhomogeneous enamel materials

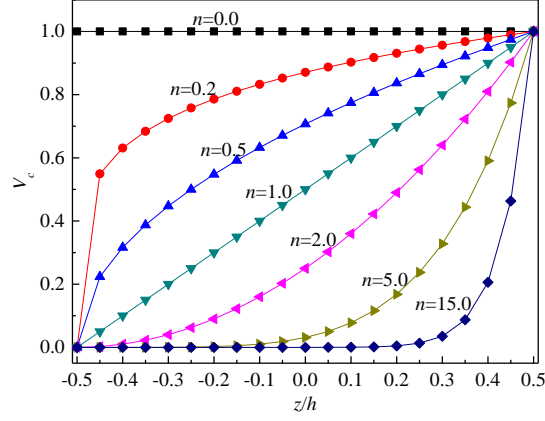


Fig. 3 Variation of volume fraction V_c function along the non-dimensional thickness with varying n

2.2 Finite element method

The elements were established by directly adopting the true parameter at the Gauss integration points of each element [59]. The equilibrium equations are given as:

$$\mathbf{K}^e \mathbf{U}^e = \mathbf{F}^e \quad (3)$$

where \mathbf{U}^e represents the nodal displacement vector and \mathbf{F}^e represents the load vector. The stiffness matrix of FEM can be expressed as:

$$\mathbf{K}^e = \int_{\Omega^e} (\mathbf{B}^e)^T \mathbf{D}^e(\mathbf{x}) \mathbf{B}^e d\Omega^e \quad (4)$$

where Ω^e represents the problem domain of finite element e , \mathbf{B}^e and $\mathbf{D}^e(\mathbf{x})$ represent the strain-displacement matrix and constitutive matrix variable, respectively. The strain-displacement is related to the gradients of the interpolating functions. In this study, the elasticity matrix $\mathbf{D}^e(\mathbf{x}) = \mathbf{D}^e(x, y)$ was assumed to be related with spatial coordinates and specified at each Gaussian integration point.

Elastic modulus E and Poisson's ratio ν in elastic matrix $\mathbf{D}^e(\mathbf{x})$ can be established by interpolation for the nonhomogeneous materials [60]:

$$E = \sum_{i=1}^{\varepsilon} N_i E_i \quad (5)$$

$$\nu = \sum_{i=1}^{\varepsilon} N_i \nu_i \quad (6)$$

where N_i denotes the FEM shape function corresponding to node i . E_i and ν_i denote the material properties at node i of the element. ε is the node number of the element. By using Eqs. (5) and (6), the actual variations of the material properties in an element can be approximated by polynomial forms.

2.3 Fracture element of enamel dumb nodes

The enamel cracks commonly seen in the clinic are closely related to the acute bite force, temperature change, and congenital developmental defects of the enamel. The properties of the mechanical field near the crack tip in nonhomogeneous enamel are the same as in homogeneous materials [61]. However, the stress intensity factors and fracture toughness parameters follow gradient functions. For VCCT, the strain energy was assumed as the same when releasing from a certain degree of crack extension or closing the crack of the same severity [54]. This reveals the similarity between crack extension from node B to C along one element and crack closure at node C (Fig. 4), which is the case of only Mode I loading.

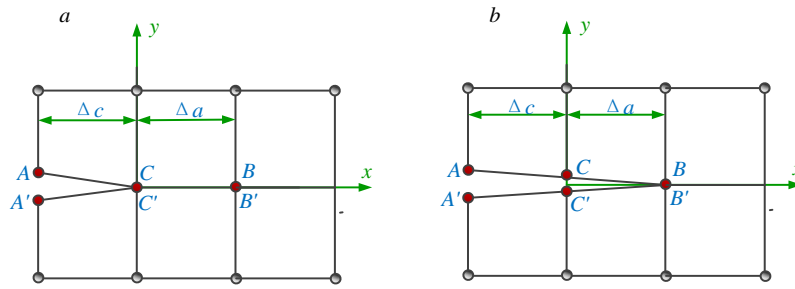


Fig. 4 Mesh configuration used for VCCT element, which describes the growth process of the crack. Crack closure at points (a) C and (b) B

Fig. 5 shows a crack inclination and crack tip with respect to the axes in the local coordinate system.

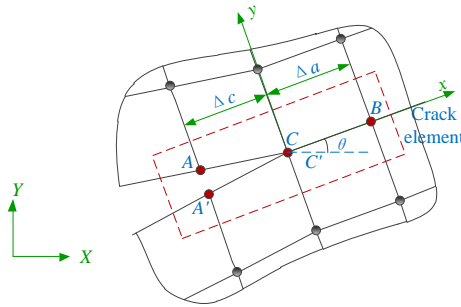


Fig. 5 Inclined crack in a plane with specific coordinates system. The crack inclination and crack tip in the local coordinate system are displayed

The details of VCCT elements can be found in Refs. [45, 62]. In particular, each element has five nodes. Nodes C and C' are located at the crack tip, node B is located ahead of the crack tip, and nodes A and A' are located behind the crack tip. The present element has two groups of nodes: a top group (nodes C , A , and B) and a bottom group (nodes C' and A'). A very stiff spring is placed between nodes C and C' , and the crack-tip nodal forces related with node displacement are given as follows:

$$F_{Cx} = K_{Cx}(u_C - u_{C'}), F_{Cy} = K_{Cy}(v_C - v_{C'}) \quad (7)$$

where (u_C, v_C) and $(u_{C'}, v_{C'})$ represent the displacement of nodes C and C' at the specific coordinate system (X, Y) , respectively; K_{Cx} and K_{Cy} represent the X - and Y -direction stiffness, respectively. Formerly, they are established with large values [45, 62], but when the crack growth is predicted, they reduce to zero.

Dummy nodes A, A', B are only employed to record the information on the displacement of the opening node behind the crack tip and the crack jump length before the tip, and do not contribute to the stiffness matrix. For nodes A and A' , the displacement openings are calculated as:

$$\Delta u = u_A - u_{A'}, \Delta v = v_A - v_{A'} \quad (8)$$

where (u_A, v_A) and $(u_{A'}, v_{A'})$ represent the displacement of nodes A and A' under the specific coordinate system (X, Y) , respectively. Hence, the crack jump length is the distance between nodes C and B , whose relation is given as follows:

$$\Delta a = \sqrt{(x_B - x_C)^2 + (y_B - y_C)^2} \quad (9)$$

where (x_C, y_C) and (x_B, y_B) are the coordinate values of nodes C and B in the global coordinate system, respectively.

The strain energy release rates (G_I and G_{II}) under the specific coordinate system (x, y) attached to the crack tip was computed. Thus, the fracture modes I and II can be separated (Fig. 5). The angle between X and x is given as:

$$\theta = \arccos\left(\frac{x_B - x_C}{\Delta a}\right) = \arcsin\left(\frac{y_B - y_C}{\Delta a}\right) \quad (10)$$

By projecting the corresponding nodal forces and crack opening displacement into specific coordinates, we can obtain:

$$\begin{pmatrix} \bar{F}_{Cx} \\ \bar{F}_{Cy} \end{pmatrix} = \begin{bmatrix} \cos \theta & \sin \theta \\ -\sin \theta & \cos \theta \end{bmatrix} \begin{pmatrix} F_{Cx} \\ F_{Cy} \end{pmatrix} \quad (11)$$

and

$$\begin{pmatrix} \Delta \bar{u}_{AA'} \\ \Delta \bar{v}_{AA'} \end{pmatrix} = \begin{bmatrix} \cos \theta & \sin \theta \\ -\sin \theta & \cos \theta \end{bmatrix} \begin{pmatrix} \Delta u_{AA'} \\ \Delta v_{AA'} \end{pmatrix} \quad (12)$$

Considering 2D-VCCT, we can express the approximate SERRs as follows:

$$G_I = \frac{\bar{F}_{Cy} \Delta \bar{v}}{2B\Delta a}, G_{II} = \frac{\bar{F}_{Cx} \Delta \bar{u}}{2B\Delta a}, \quad (13)$$

where B represents the structure thickness.

For the analysis of the dynamic loading fixed crack problem, we can describe the relationship between dynamic stress intensity factors K_I (K_{II}) and strain energy release rates G_I (G_{II}) as follows:

$$K_I = \text{sign}(\bar{F}_{Cy}) \sqrt{\bar{E}G_I} \quad (14)$$

$$K_{II} = \text{sign}(\bar{F}_{Cx}) \sqrt{\bar{E}G_{II}} \quad (15)$$

where \bar{E} represents material matrix and has different expressions in plane stress and plane strain conditions (plane stress $\bar{E} = E^{tip}$, plane strain condition: $\bar{E} = \frac{E^{tip}}{1 - (\mu^{tip})^2}$); E^{tip} and μ^{tip} denote the crack tip elasticity modulus and crack tip Poisson's ratio, respectively [63].

3. RESULTS AND DISCUSSION

3.1 Example 1

Given the problem of central enamel cracks, we have selected finite-width central crack tension trials. The geometric model and the loading are shown in Fig. 6, where L , W , and B represent length, width, and thickness of the model, respectively ($L=2$ mm, $W=2$ mm, $B=0.1$ mm). The crack length was $2a$ and the tension load is $\sigma=30$ MPa. The enamel is composed of materials M and C. The two materials were subjected to Eqs. (1) and (2), where the power exponent factors were $n=0, 0.5, 1.0, 5.0$ and the elastic moduli were $M_m=90$ GPa and $M_c=120$ GPa. These two materials had the same Poisson's ratio $\nu=0.3$ (the properties of the enamel are the same in other examples).

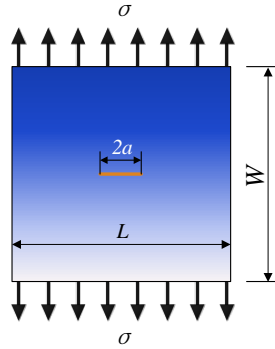


Fig. 6 Geometric model of an enamel specimen containing a central crack

To illustrate the convergence of this method, we have simulated a discrete model of 4 element meshes to the normalized DSIFs K_I (40×40 elements, 80×80 elements, 120×120 elements). The model was geometrically established with 2D CPE4 (2D standard plane strain elements) in ABAQUS®. We have employed no special means, such as the collapsed element technique at the crack tip or special singular elements. Table 1 shows energy release rate G_I from the computation model with power exponent factors $n=0.0, 0.5, 1.0,$ and 5.0 , four grids, and crack lengths $a=0.2, 0.3, 0.4, 0.5,$ and 0.6 mm. By comparing with the analytical solutions, we validated the accuracy and effectiveness of the new method.

Fig. 7 shows energy release rate G_I computed from the model with power exponent factors $n=0.0, 0.5, 1.0,$ and 5.0 , crack lengths $a=0.3, 0.4, 0.5,$ and 0.6 mm, and cell division = 100×100 . Compared with the analytical solutions, the maximum error was only 3.2%, which indicates that the nonhomogeneous enamel calculation model and the calculation method proposed in this study is accurate and effective.

Table 1 Energy release rate G_I (N/mm) computed from the new model at power exponent factors of $n=0.0, 0.5, 1.0,$ and 5.0

n	Method	a (mm)				
		0.2	0.3	0.4	0.5	0.6
0.0	VCCT 120×120	0.00485	0.00792	0.01212	0.01856	0.02664
	VCCT 80×80	0.00484	0.00791	0.01202	0.01863	0.02687
	VCCT 40×40	0.00480	0.00790	0.01208	0.01838	0.02681
	Anal. solu.	0.00496	0.00807	0.01235	0.01896	0.02731
0.5	VCCT 120×120	0.00535	0.00854	0.01301	0.02006	0.02887
	VCCT 80×80	0.00526	0.00852	0.01303	0.01999	0.02901
	VCCT 40×40	0.00524	0.00851	0.01297	0.02016	0.02898
	Anal. solu.	0.00535	0.00871	0.01333	0.02046	0.02947
1.0	VCCT 120×120	0.00552	0.00901	0.01376	0.02116	0.03056
	VCCT 80×80	0.00555	0.00903	0.01372	0.02113	0.03053
	VCCT 40×40	0.00553	0.00904	0.01381	0.02130	0.03062
	Anal. solu.	0.00566	0.00922	0.01411	0.02167	0.03121
5.0	VCCT 120×120	0.00637	0.01062	0.01598	0.02435	0.03511
	VCCT 80×80	0.00633	0.01043	0.01596	0.02433	0.03503
	VCCT 40×40	0.00637	0.01039	0.01599	0.02448	0.03532
	Anal. solu.	0.00651	0.01065	0.01632	0.02504	0.03608

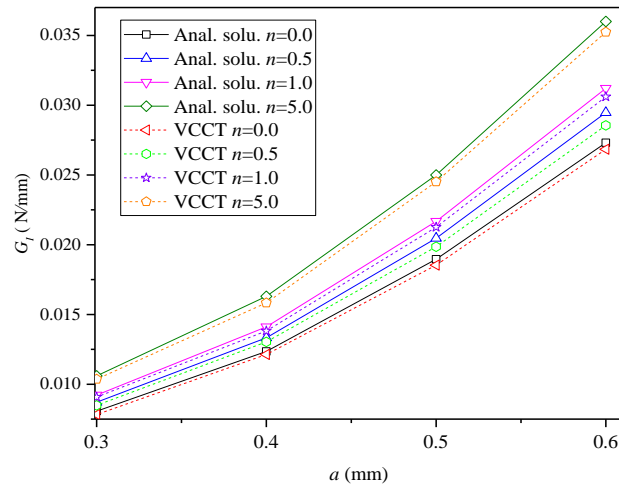


Fig. 7 Energy release rate G_I at crack lengths $a= 0.3, 0.4, 0.5,$ and 0.6 mm with different power exponent factors $n=0.0, 0.5, 1.0,$ and 5.0

3.2 Example 2

Given the three-point bending problems of enamel, we have conducted three-point bending trials. The geometric model with length $W=4.4$ mm, width $H=1$ mm, span $S=4$ mm, thickness $B=0.25$ mm is shown in Fig. 8, where a denotes the length of the crack. The model is subject to a concentrated load P of 1.0 N.

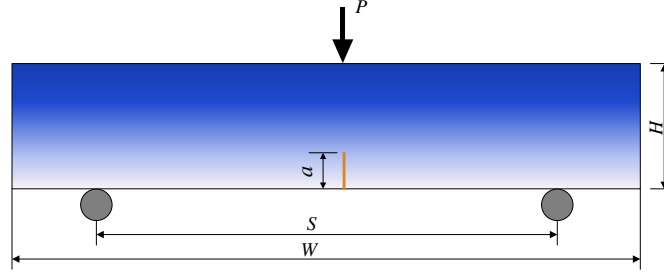


Fig. 8 Enamel specimens for three-point bending trials

Fig. 9 shows energy release rate G_I with power exponent factors $n=0.0, 0.5, 1.0,$ and 5.0 and crack lengths $a=0.45, 0.50, 0.55,$ and 0.6 mm. Compared with the analytical solutions, the maximum error was only 3.9%, indicating that the nonhomogeneous enamel computation model and the method proposed are accurate and effective.

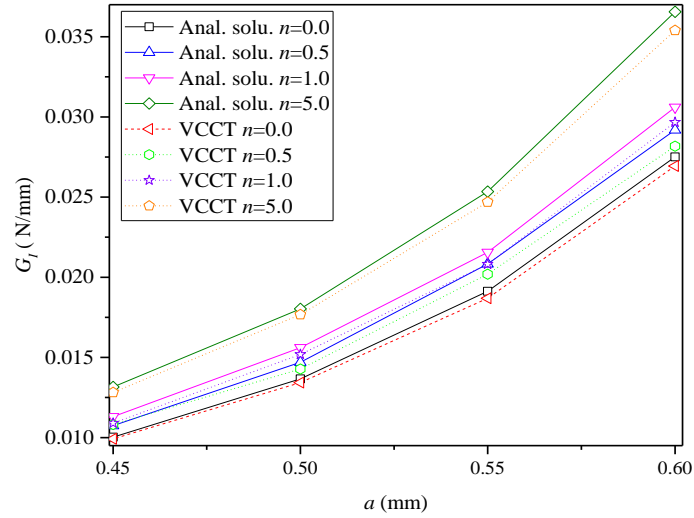


Fig. 9 Energy release rate G_I of three-point bending enamel specimens at crack lengths $a=0.45, 0.50, 0.55,$ and 0.6 mm with different power exponent factors $n=0.0, 0.5, 1.0,$ and 5.0

3.3 Example 3

In the enamel compact tensile trials, the geometric model and loading are shown in Fig. 10, where L , W , and B represent length, width, and thickness of the model, respectively ($L=1$ mm, $W=1.25$ mm, $B=0.1$ mm). The crack length is a and $P=1.0$ N is a concentrated load.

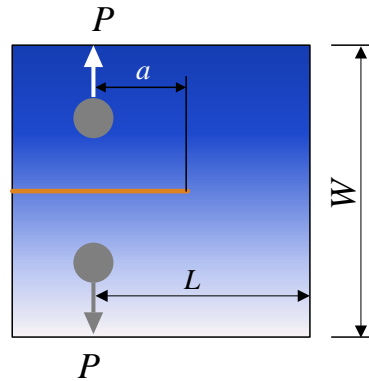


Fig. 10 Enamel specimen for compact tensile trials

Fig. 11 demonstrates energy release rate G_I computed from power exponent factors $n=0.0, 0.5, 1.0$, and 5.0 , and crack lengths $a=0.3, 0.4, 0.5$, and 0.6 mm. Compared with the analytical solutions, the maximum error was only 3.3%, indicating that the nonhomogeneous enamel computation model and the method proposed are accurate and effective.

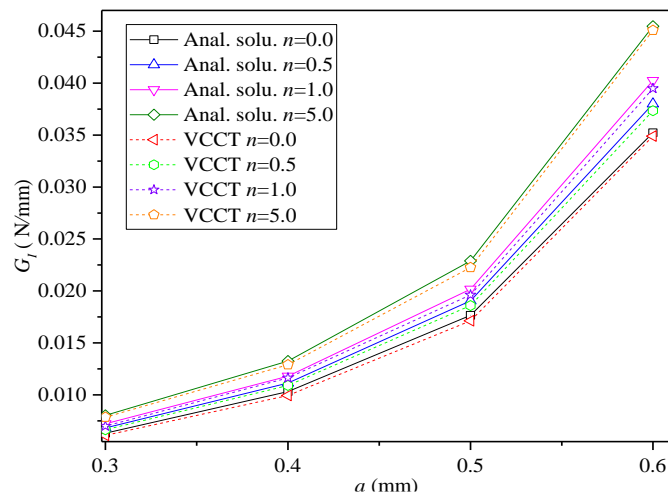


Fig. 11 Energy release rate G_I from compact tension enamel specimens at crack lengths $a=0.3, 0.4, 0.5$, and 0.6 mm with different power exponent factors $n=0.0, 0.5, 1.0$, and 5.0

3.4 Example 4

The geometric model and loading for double-edge-notched tension tests are shown in Fig. 12, where L , W , and B represent length, width, and thickness of the model, respectively ($L=2$ mm, $W=2$ mm, $B=0.1$ mm). The crack length is a , and the load $\sigma=40$ MPa is uniformly distributed.

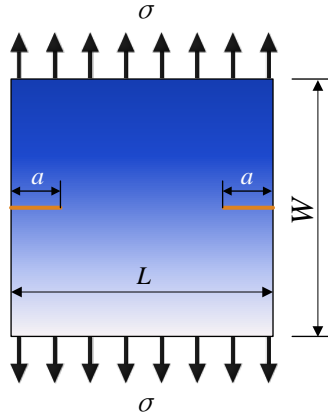


Fig. 12 Enamel specimens for double-edge-notched tension tests

Fig. 13 shows energy release rate G_I computed at power exponent factors $n=0.0, 0.5, 1.0,$ and 5.0 and crack lengths $a=0.2, 0.3, 0.4,$ and 0.5 mm. Compared with the analytical solutions, the maximum error was only 4.1%, indicating that the nonhomogeneous enamel computation model and the method proposed are accurate and effective.

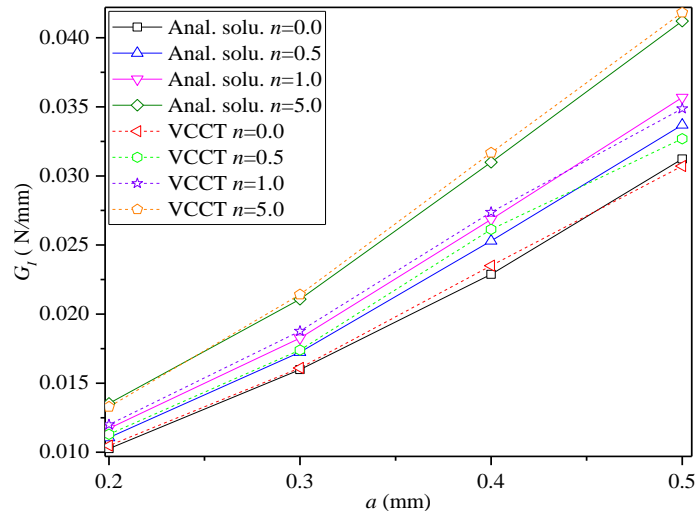


Fig. 13 Energy release rate G_I from compact tension enamel specimens at crack lengths $a=0.2, 0.3, 0.4,$ and 0.5 mm

4. CONCLUSIONS

Based on FEM, the 2D-VCCT enamel dumb element was constructed, which can be employed in the fracture analysis of enamel. We implemented the element into ABAQUS by the user element subroutine (UMAT and UEL). In view of the numerical examples, the results were in agreement with the analytical solutions, which verified that this proposed interface element can directly apply fracture mechanics to solve fracture problems on ABAQUS. The proposed element has some advantages, such as the ability to extract fracture parameters without extra post-processing while the definition of body mesh is unconstrained. The proposed element can also be integrated with FEM. Thus, as the reliability of the proposed element was proved in various cases, it can be potentially employed in nonhomogeneous material fractures. In summary, the proposed method is simple, efficient, universal, and steady, and can be applied to the structure-level analysis of nonhomogeneous fracturing problems by resorting to the commercial FEA codes.

Acknowledgments: *The authors are grateful for the financial support to the National Natural Science Foundation of China (grant no. 51975243), Scientific Research Project of Jilin Provincial Department of Education (grant no. JJKH20190131KJ) and Graduate Innovation Fund of Jilin University (grant no. 101832020CX099).*

REFERENCES

1. Schwartz, G.T., 2000, *Enamel thickness and the helicoidal wear plane in modern human mandibular molars*, Archives of Oral Biology, 45(5), pp. 401-409.
2. Sajewicz, E., 2006, *On evaluation of wear resistance of tooth enamel and dental materials*, Wear, 260(11-12), pp. 1256-1261.
3. Bairo, F., Verne, E., 2017, *Production and Characterization of Glass-Ceramic Materials for Potential Use in Dental Applications: Thermal and Mechanical Properties, Microstructure, and In Vitro Bioactivity*, Applied Sciences, 7(12), 1330.
4. Zhao, X.L., O'Brien S., Shaw, J., Abbott, P., Munroe, P., Habibi, D., Xie, Z.H., 2013, *The origin of remarkable resilience of human tooth enamel*, Applied Physics Letters, 103(24), 241901.
5. Cui, F.Z., Ge, J., 2007, *New observations of the hierarchical structure of human enamel, from nanoscale to microscale*, Journal of Tissue Engineering and Regenerative Medicine, 1(3), pp. 185-191.
6. Nanci, A., 2008, *Ten Cate's Oral Histology: Development, Structure, and Function, 8th ed*, Elsevier, Missouri, US.
7. He, L.H., Swain M.V., 2008, *Understanding the mechanical behaviour of human enamel from its structural and compositional characteristics*, Journal of the Mechanical Behavior of Biomedical Materials, 1(1), pp. 18-29.
8. Gao, X., Qin, W., Wang, P., Wang, L., Weir, M., Reynolds, M.A., Zhao, L., Lin, Z.M., Xu, H., 2019, *Nano-Structured Demineralized Human Dentin Matrix to Enhance Bone and Dental Repair and Regeneration*, Applied Sciences, 9(5), 1013.
9. Lubisich, E.B., Hilton, T.J., Ferrancane, J., Peregcent, N., 2010, *Cracked Teeth: A Review of the Literature*, Journal of Esthetic and Restorative Dentistry, 22(3), pp. 158-167.
10. Chai, H., Lee, J.J.W., Constantino, P.J., Lucas, P.W., Lawn, B.R., 2009, *Remarkable resilience of teeth*, Proceedings of the National Academy of Sciences of the United States of America, 106(18), pp. 7289-7293.
11. Chai, H., Lee, J.J.W., Kwon, J.Y., Lucas, P.W., Lawn, B.R., 2009, *A simple model for enamel fracture from margin cracks*, Acta Biomaterialia, 5(5), pp. 1663-1667.
12. Lawn, B.R., Lee, J.J.W., 2009, *Analysis of fracture and deformation modes in teeth subjected to occlusal loading*, Acta Biomaterialia, 5(6), pp. 2213-2221.

13. Kato, H., Taguchi, Y., Imai, K., Ruan, Y., Tsai, Y.W., Chen, Y.C., Shida, M., Taguchi, R., Tominaga, K., Umeda, M., 2018, *The enhancing effects of amelogenin exon 5-encoded peptide from enamel matrix derivative on odontoblast-like KN-3 cells*, Applied Sciences, 8(10), 1890.
14. Lara-Carrillo, E., Lovera-Roias, N., Luckie, R.A.M., Robles, L., Garcia-Fabila, M.M., Rosa-Santillana, R., Medina-Solis, C.E., 2018, *The effects of remineralization via fluoride versus low-level laser IR810 and fluoride agents on the mineralization and microhardness of bovine dental enamel*, Applied Sciences, 8(1), 78.
15. Meredith, N., Sherriff, M., Setchell, D.J., Swanson, S.A.V., 1996, *Measurement of the microhardness and Young's modulus of human enamel and dentine using an indentation technique*, Archives of Oral Biology, 41(6), pp. 539-545.
16. Wegest, U.G.K., Bai, H., Saiz, E., Tomsia, A.P., Ritchie, R.O., 2015, *Bioinspired structural materials*, Nature Materials, 14(1), pp. 23-36.
17. Cuy, J.L., Mann, A.B., Livi, K.J., Teaford, M.F., Weihs, T.P., 2002, *Nanoindentation mapping of the mechanical properties of human molar tooth enamel*, Archives of Oral Biology, 47(4), pp. 281-291.
18. Braly, A., Darnell, L.A., Mann, A.B., Teaford, M.F., Weihs, T.P., 2007, *The effect of prism orientation on the indentation testing of human molar enamel*, Archives of Oral Biology, 52(9), pp. 856-860.
19. Park, S., Wang, D.H., Zhang, D.S., Romberg, E., Arola, D., 2008, *Mechanical properties of human enamel as a function of age and location in the tooth*, Journal of Materials Science-Materials in Medicine, 19(6), pp. 2317-2324.
20. Habelitz, S., Marshall, S.J., Marshall, G.W., Balooch, M., 2001, *Mechanical properties of human dental enamel on the nanometre scale*, Archives of Oral Biology, 46(2), pp. 173-183.
21. Balooch, G., Marshall, G.W., Marshall, S.J., Warren, O.L., Asif, S.A.S., Bolooch, M., 2004, *Evaluation of a new modulus mapping technique to investigate microstructural features of human teeth*, Journal of Biomechanics, 37(8), pp. 1223-1232.
22. He, L.H., Fujisawa, N., Swain, M.V., 2006, *Elastic modulus and stress-strain response of human enamel by nano-indentation*, Biomaterials, 27(24), pp. 4388-4398.
23. Mann, A.B., Dickinson, M.E., 2006, *Nanomechanics, chemistry and structure at the enamel surface*, Monographs in Oral Science, 19, pp. 105-131.
24. Bajaj, D., Arola, D.D., 2009, *On the R-curve behavior of human tooth enamel*, Biomaterials, 30(23-24), pp. 4037-4046.
25. Liu, P.F., Hou, S.J., Chu, J.K., Hu, X.Y., Zhou, C.L., Liu, Y.L., Zheng, J.Y., Zhao, A., Yan, L., 2011, *Finite element analysis of postbuckling and delamination of composite laminates using virtual crack closure technique*, Composite Structures, 93(6), pp. 1549-1560.
26. Sun, L., Ma, D.J., Wang, L.Z., Shi, X.Z., Wang, J.L., Chen, W., 2018, *Determining indentation fracture toughness of ceramics by finite element method using virtual crack closure technique*, Engineering Fracture Mechanics, 197, pp. 151-159.
27. Sun, Z.Z., Zhang, X.Y., Zhang, Y.M., 2019, *Cracking elements method for simulating complex crack growth*, Journal of Applied and Computational Mechanics, 5(3), pp. 552-562.
28. Zmudzki, J., Chladek, G., Krawczyk, C., 2019, *Relevance of Tongue Force on Mandibular Denture Stabilization during Mastication*, Journal of Prosthodontics-Implant Esthetic and Reconstructive Dentistry, 28(1), pp. E27-E33.
29. Zmudzki, J., Chladek, G., Malara, P., 2018, *Use of finite element analysis for the assessment of biomechanical factors related to pain sensation beneath complete dentures during mastication*, Journal of Prosthetic Dentistry, 120(6), pp. 934-941.
30. Zmudzki, J., Chladek, G., Panek, K., Lipinski, P., 2020, *Finite element analysis of adolescent mandible fracture occurring during accidents*, Archives of Metallurgy and Materials, 65(1), pp. 65-72.
31. Nehdi, M.L., Ali, M.A.E.M., 2019, *Experimental and numerical study of engineered cementitious composite with strain recovery under impact loading*, Applied Sciences, 9(5), pp. 994.
32. Shabani, S., Cunedioğlu, Y., 2019, *Free vibration analysis of functionally graded beams with cracks*, Journal of Applied and Computational Mechanics, 6(4), pp. 908-919.
33. Zenkour, A.M., Abouelregal, A.E., 2019, *Fractional thermoelasticity model of a 2D problem of mode-I crack in a fibre-reinforced thermal environment*, Journal of Applied and Computational Mechanics, 5(2), pp. 269-280.
34. Cui, W., Zhang, Y.H., Xiao, Z.M., Zhang, Q., 2020, *A new magnetic structural algorithm based on virtual crack closure technique and magnetic flux leakage testing for circumferential symmetric double-crack propagation of X80 oil and gas pipeline weld*, Acta Mechanica, 231(3), pp. 1187-1207.

35. Fang, G., Li, L., Gao, X.G., Song, Y.D., 2020, *Finite element analysis of the crack deflection in fiber reinforced ceramic matrix composites with multilayer interphase using virtual crack closure technique*, Applied Composite Materials, 27(3), pp. 307-320.
36. Zhang, W., Jiang, W.C., Yu, Y., Zhou, F., Luo, Y., Song, M., 2019, *Fatigue crack simulation of the 316L brazed joint using the virtual crack closure technique*, International Journal of Pressure Vessels and Piping, 173, pp. 20-25.
37. Zhao, Y., Sun, X.J., Cao, P., Ling, Y.F., Gao, Z., Zhan, Q.B., Zhou, X.J., Diao, M.S., 2019, *Mechanical performance and numerical simulation of basalt fiber reinforced concrete (BFRC) using double-K Fracture model and virtual crack closure technique (VCCT)*, Advances in Civil Engineering, 2019, 5630805.
38. Chiu, T.C., Lin, H.C., 2009, *Analysis of stress intensity factors for three-dimensional interface crack problems in electronic packages using the virtual crack closure technique*, International Journal of Fracture, 156(1), pp. 75-96.
39. Scheel, J., Ricoeur, A., Krupka, M., 2019, *Calculation of stress intensity factors with an analytical enrichment of the modified crack closure integral*, 25th International Conference on Fracture and Structural Integrity, 18, pp. 268-273.
40. Zhao, X., Mo, Z.L., Guo, Z.Y., Li, J., 2020, *A modified three-dimensional virtual crack closure technique for calculating stress intensity factors with arbitrarily shaped finite element mesh arrangements across the crack front*, Theoretical and Applied Fracture Mechanics, 109, 102695.
41. Parashar, A., Mertiny, P., 2012, *Study of mode I fracture of graphene sheets using atomistic based finite element modeling and virtual crack closure technique*, International Journal of Fracture, 176(1), pp. 119-126.
42. Zhang, H., Qiao, P.Z., 2020, *Virtual crack closure technique in peridynamic theory*, Computer Methods in Applied Mechanics and Engineering, 372, 113318.
43. Heidari-Rarani, M., Sayedain, M., 2019, *Sayedain, Finite element modeling strategies for 2D and 3D delamination propagation in composite DCB specimens using VCCT, CZM and XFEM approaches*, Theoretical and Applied Fracture Mechanics, 103, 102246.
44. Xie, D., Biggers, S.B., 2006, *Progressive crack growth analysis using interface element based on the virtual crack closure technique*, Finite Elements in Analysis and Design, 42(11), pp. 977-984.
45. Ikeda, T., Sun, C.T., 2001, *Stress intensity factor analysis for an interface crack between dissimilar isotropic materials under thermal stress*, International Journal of Fracture, 111(3), pp. 229-249.
46. Farkash, E., Banks-Sills, L., 2017, *Virtual crack closure technique for an interface crack between two transversely isotropic materials*, International Journal of Fracture, 205(2), pp. 189-202.
47. Heidari-Rarani, M., Sayedain, M., 2019, *Finite element modeling strategies for 2D and 3D delamination propagation in composite DCB specimens using VCCT, CZM and XFEM approaches*, Theoretical and Applied Fracture Mechanics, 103, 5630805.
48. Krueger, R., 2004, *Virtual crack closure technique: History, approach, and applications*, Applied Mechanics Reviews, 57(2), pp. 109-143.
49. Leski, A., 2007, *Implementation of the virtual crack closure technique in engineering FE calculations*, Finite Elements in Analysis and Design, 43(3), pp. 261-268.
50. Azimi, M., Mirjavadi, S.S., Asli, S.A., Hamouda, A.M.S., 2017, *Fracture analysis of a special cracked lap shear (CLS) specimen with utilization of virtual crack closure technique (VCCT) by finite element methods*, Journal of Failure Analysis and Prevention, 17(2), pp. 304-314.
51. Zeng, W., Liu, G.R., Jiang, C., Dong, X.W., Chen, H.D., Bao, Y., Jiang, Y., 2016, *An effective fracture analysis method based on the virtual crack closure-integral technique implemented in CS-FEM*, Applied Mathematical Modelling, 40(5-6), pp. 3783-3800.
52. Banks-Sills, L., Farkash, E., 2016, *A note on the virtual crack closure technique for a bimaterial interface crack*, International Journal of Fracture, 201(2), pp. 171-180.
53. Muthu, N., Falzon, B.G., Maiti, S.K., Khoddam, S., 2014, *Modified crack closure integral technique for extraction of SIFs in meshfree methods*, Finite Elements in Analysis and Design, 78, pp. 25-39.
54. Zhou, L.M., Meng, G.W., Li, X.L., Li, F., 2016, *Analysis of dynamic fracture parameters in functionally graded material plates with cracks by graded finite element method and virtual crack closure technique*, Advances in Materials Science and Engineering, 2016, 8085107.
55. Santare, M.H., Thamburaj, P., Gazonas, G.A., 2003, *The use of graded finite elements in the study of elastic wave propagation in continuously nonhomogeneous materials*, International Journal of Solids and Structures, 40(21), pp. 5621-5634.

56. Anlas, G., Santare, M.H., Lambros, J., 2000, *Numerical calculation of stress intensity factors in functionally graded materials*, International Journal of Fracture, 104(2), pp. 131-143.
57. Hagemann, A., Rohr, K., Stiehl, H.S., 2002, *Coupling of fluid and elastic models for biomechanical simulations of brain deformations using FEM*, Medical Image Analysis, 6(4), pp. 375-388.
58. Kim, J.H., Paulino, G.H., 2002, *Mixed-mode fracture of orthotropic functionally graded materials using finite elements and the modified crack closure method*, Engineering Fracture Mechanics, 69(14-16), pp. 1557-1586.
59. Santare, M.H., Lambros, J., 2000, *Use of graded finite elements to model the behavior of nonhomogeneous materials*, Journal of Applied Mechanics-Transactions of the Asme, 67(4), pp. 819-822.
60. Li, C.Y., Zou, Z.Z., Duan, Z.P., 2000, *Multiple isoparametric finite element method for nonhomogeneous media*, Mechanics Research Communications, 27(2), pp. 137-142.
61. Dolbow, J.E., Gosz, M., 2002, *On the computation of mixed-mode stress intensity factors in functionally graded materials*, International Journal of Solids and Structures, 39(9), pp. 2557-2574.
62. Qian, Q., Xie, D., 2007, *Analysis of mixed-mode dynamic crack propagation by interface element based on virtual crack closure technique*, Engineering Fracture Mechanics, 74(5), pp. 807-814.
63. Yang, Z.J., Yao, F., Huang, Y.J., 2020, *Development of ABAQUS UEL/VUEL subroutines for scaled boundary finite element method for general static and dynamic stress analyses*, Engineering Analysis with Boundary Elements, 114, pp. 58-73.